JOURNAL OF GEOPHYSICAL RESEARCH, VOL. 108, NO. D14, 4414, doi:10.1029/2002JD002654, 2003

Effects of land use in Southwest Australia: 1. Observations of cumulus cloudiness and energy fluxes

Deepak K. Ray,[1] Udaysankar S. Nair,[1] Ronald M. Welch,[1] Qingyuan Han,[1] Jian Zeng,[1] Wenying Su,[2] Tokio Kikuchi,[3] and Tom J. Lyons[4]

Received 14 June 2002; revised 15 October 2002; accepted 17 March 2003; published 22 July 2003.

[1] The Southwest Australian region has large homogeneous tracts of differing vegetation types separated by a sharp transition called the vermin or bunny fence which runs for almost 750 km. Seasonal winter agriculture is found to the west of the fence, whereas to the east native perennial vegetation grows. Geostationary Meteorological Satellite-5 imagery are used to construct monthly cumulus cloud frequency of occurrence maps for the region 0800 to 1500 LT in hourly increments for 1999 and 2000. Moderate Resolution Imaging Spectroradiometer (MODIS) imagery are used to retrieve regional values of surface temperature, albedo, Normalized Difference Vegetation Index, fractional soil moisture availability, sensible and latent heat fluxes. High spatial resolution Advanced Spaceborne Thermal Emission and Reflection Radiometer (ASTER) imagery are used to retrieve detailed values along the fence. MODIS imagery also is utilized to retrieve cloud optical thickness, droplet sizes, and liquid water paths. This study shows that higher soil moisture availability is found over agricultural areas during winter (September) and over native vegetation areas during summer (December). Latent heat fluxes are higher over native vegetation than over agricultural areas during summer, while sensible heat fluxes are lower. Cumulus clouds occur with higher frequency and have higher optical thicknesses, cloud liquid water contents, and effective radii over agricultural areas during the winter and over native perennial vegetation during the dry summer. This is due to higher latent heat fluxes and available energy over agriculture during winter and over native vegetation during summer. We conclude that land use differences result in differences in available soil moisture and surface energy fluxes, which in turn lead to the observed preferential enhancement of cumulus cloudiness and cumulus cloud properties. *INDEX TERMS:* 3322 Meteorology and Atmospheric Dynamics: Land/atmosphere interactions; 3360 Meteorology and Atmospheric Dynamics: Remote sensing; 3309 Meteorology and Atmospheric Dynamics: Climatology (1620); 3314 Meteorology and Atmospheric Dynamics: Convective processes; 3359 Meteorology and Atmospheric Dynamics: Radiative processes; *KEYWORDS:* land-atmosphere interaction, soil moisture, surface energy fluxes, land use, cloud formation, cloud properties

Citation: Ray, D. K., U. S. Nair, R. M. Welch, Q. Han, J. Zeng, W. Su, T. Kikuchi, and T. J. Lyons, Effects of land use in Southwest Australia: 1. Observations of cumulus cloudiness and energy fluxes, *J. Geophys. Res.*, *108*(D14), 4414, doi:10.1029/2002JD002654, 2003.

1. Introduction

[2] Land use greatly influences regional climate by modulating the surface energy budget. Characteristics of the landscape, such as vegetation cover, soil type, surface roughness, soil moisture distribution, albedo, and temperature, control the magnitude of surface energy fluxes [*Pielke*, 2001]. Variations in surface properties, therefore, can produce changes in boundary layer air temperature and moisture, the depth of the boundary layer, cloudiness, and local rainfall [*Segal et al.*, 1988; *Meher-Homji*, 1991; *Sud et al.*, 1993; *Pielke*, 2001]. In particular, the nature of land use can have a significant influence on the preferential formation and development of convective clouds due to modification of thermodynamic properties of air masses above contrasting vegetation types.

[3] *Rabin* [1977] used a surface energy budget model to study the effect of vegetation and soil moisture on the timing of convective storm initiation. Noticeable modulation of convection by the land surface was observed when the synoptic forcing was weak. Their results showed that convective cumulus clouds formed earliest over regions characterized by high sensible heat flux and were suppressed over regions characterized by high latent heat flux. Such prefer-

[1]Department of Atmospheric Sciences, University of Alabama in Huntsville, Huntsville, Alabama, USA.
[2]Center for Atmospheric Sciences, Hampton University, Hampton, Virginia, USA.
[3]Department of Information Science, Kochi University, Kochi City, Japan.
[4]School of Environmental Science, Murdoch University, Murdoch, Western Australia, Australia.

0148-0227/03/2002JD002654$09.00

ential formation of cumulus clouds also was observed over deforested regions in Amazonia [*Cutrim et al.*, 1995] and over areas of relatively sparse vegetation cover in central United States [*Rabin and Martin*, 1996]. On the other hand, *Segal et al.* [1995] suggested that latent heat flux is the dominant forcing in destabilization, with sensible heat flux in the secondary role, because drier surfaces are less conducive to deep convection even though the associated boundary layer is deeper. Likewise, *Lynn et al.* [1998] suggested that the largest potential for deep convection is over wet ground. *Rabin et al.* [1990] reported that differences in atmospheric thermodynamic properties, related to the differences in the nature of underlying land use, may result in the preferential formation of convective clouds over certain regions. *Pielke* [2001] provides a detailed review of the influence of vegetation and soil properties on cumulus cloudiness and rainfall.

[4] Several modeling and theoretical studies [*Segal et al.*, 1988; *Avissar and Liu*, 1996; *Avissar and Schmidt*, 1998; *Weaver and Avissar*, 2001] have shown that differential heating over contrasting surface types, such as vegetated areas adjacent to dry bare soil, results in the generation of sea-breeze-like mesoscale circulations. These models assumed that the contrasting surface types were spatially extensive. However, *Zhong and Doran* [1998] disagreed that modeling studies could simulate real-world thermally induced circulations. They note that the studies not only use idealized land surface conditions, but most of these studies also use idealized atmospheric conditions. In contrast, the Southwest Australian region under consideration has large, relatively homogeneous tracts of differing vegetation types and no significant topographical variations. Therefore the land surface heterogeneity in this region is similar to those assumed in the modeling studies discussed above.

[5] Figure 1a shows the region of interest in this study, lying between latitude 26°–36°S and longitude 114°–124°E, in Southwest Australia. Figure 1b shows Geostationary Meteorological Satellite-5 (GMS5) visible channel imagery for this region on 3 January 1999. Note the presence of large, relatively homogeneous tracts of land, with native vegetation to the east and a wheat belt to the west of a sharp transition almost 750 km long called the bunny or vermin fence. The vermin fence was erected for protecting the wheat and barley crops from rabbits, and it marks the eastern boundary of the areas cleared for agricultural use. Figure 1c shows a collocated Moderate Resolution Imaging Spectroradiometer (MODIS) channel 1 (0.65 μm) image of this area, with the locations of the six Advanced Spaceborne Thermal Emission and Reflection Radiometer (ASTER) images used in this study. Table 1 lists the dates and times that the ASTER data were acquired. Figure 1d shows the high-resolution channel 1 (0.56 μm) image of the subregion 2 outlined in Figure 1c. The ASTER image shows that the actual boundary between the vegetation types projects into each other and is not as sharply demarcated as indicated in Figures 1a, 1b, and 1c.

[6] The creation of such a landscape in Southwest Australia is the culmination of considerable land use change since the late 1800s. An estimated 13 million hectares of native perennial vegetation has been cleared since the beginning of the century for winter growing agricultural crops. Following the substantial clearing of native vegetation, a 20% decline in local winter rainfall also has been reported [*Lyons et al.*, 1993]. In order to understand the impact of these large-scale land use changes upon regional climate as well as their impact upon regional cloudiness, aircraft and satellite measurements have been made of surface properties [*Lyons et al.*, 1993, 1996], and surface energy fluxes have been computed from models [*Huang et al.*, 1995]. *Lyons et al.* [1996] used Advanced Very High Radiance Radiometer (AVHRR) satellite data to determine the net radiation and ground heat flux at approximately 1430 LT and then used prescribed Bowen ratios to partition available energy into latent and sensible heat fluxes. In contrast, *Huang et al.* [1995] used a one-dimensional (1-D) boundary layer model to derive the daily accumulation of surface energy fluxes. In addition, aircraft measurements of latent and sensible heat fluxes have been taken at various periods during the day from 24 to 30 September 1992 and from 4 to 6 October 1993 during the Bunny Fence Experiment (buFex). The aircraft measured values reported during buFex were averaged over 20 km segments on both sides of the fence.

[7] Based upon AVHRR data near 1430 LT, *Lyons et al.* [1996] found that sensible heat fluxes are larger over native vegetation than over agricultural regions in all seasons; latent heat fluxes were higher over native vegetation during summer and over agriculture during winter. *Lyons et al.* [1993] suggested the higher sensible heat fluxes and the resultant vigorous mixing in the boundary layer to be responsible for the observed preferential cloud formation over native vegetation. On the other hand, the aircraft observations during late September-early October show that latent heat fluxes are significantly larger than sensible heat fluxes during daylight hours over agricultural areas (Bowen ratios usually >1.5); over native vegetation latent heat fluxes are greater than sensible heat fluxes in the morning and late afternoon hours, but then smaller than sensible heat fluxes (Bowen ratios often <0.67) during the heat of the day.

[8] In Part 1 of this series, results are presented for seasonal variations (from the August growing season to the height of summer in December) of land surface properties, such as fractional soil moisture availability, surface energy fluxes, and cumulus cloudiness. Seasonal variations in cumulus cloud optical and microphysical properties also are examined in order to determine whether the seasonal changes in land use influence cumulus cloud properties. The Part 2 study will examine the effects of land use on the regional climate and precipitation patterns using a 3-D mesoscale model; in addition, Tropical Rainfall Measuring Mission (TRMM) data will be used to examine satellite-derived estimates of precipitation, and Clouds and the Radiant Energy System (CERES) measurements will be used to retrieve surface energy budgets.

[9] Section 2 of this paper describes the data sets used in this study. Section 3 discusses the methodology. Section 4 deals with the results obtained from this study, and section 5 concludes.

2. Data

[10] Table 2 shows the locations of four Southwest Australian stations from which radiosonde data were obtained for this study. These data sets are used to initialize the Soil Vegetation Atmospheric Transfer (SVAT) model [*Gillies et al.*, 1997], which is used for retrieving available

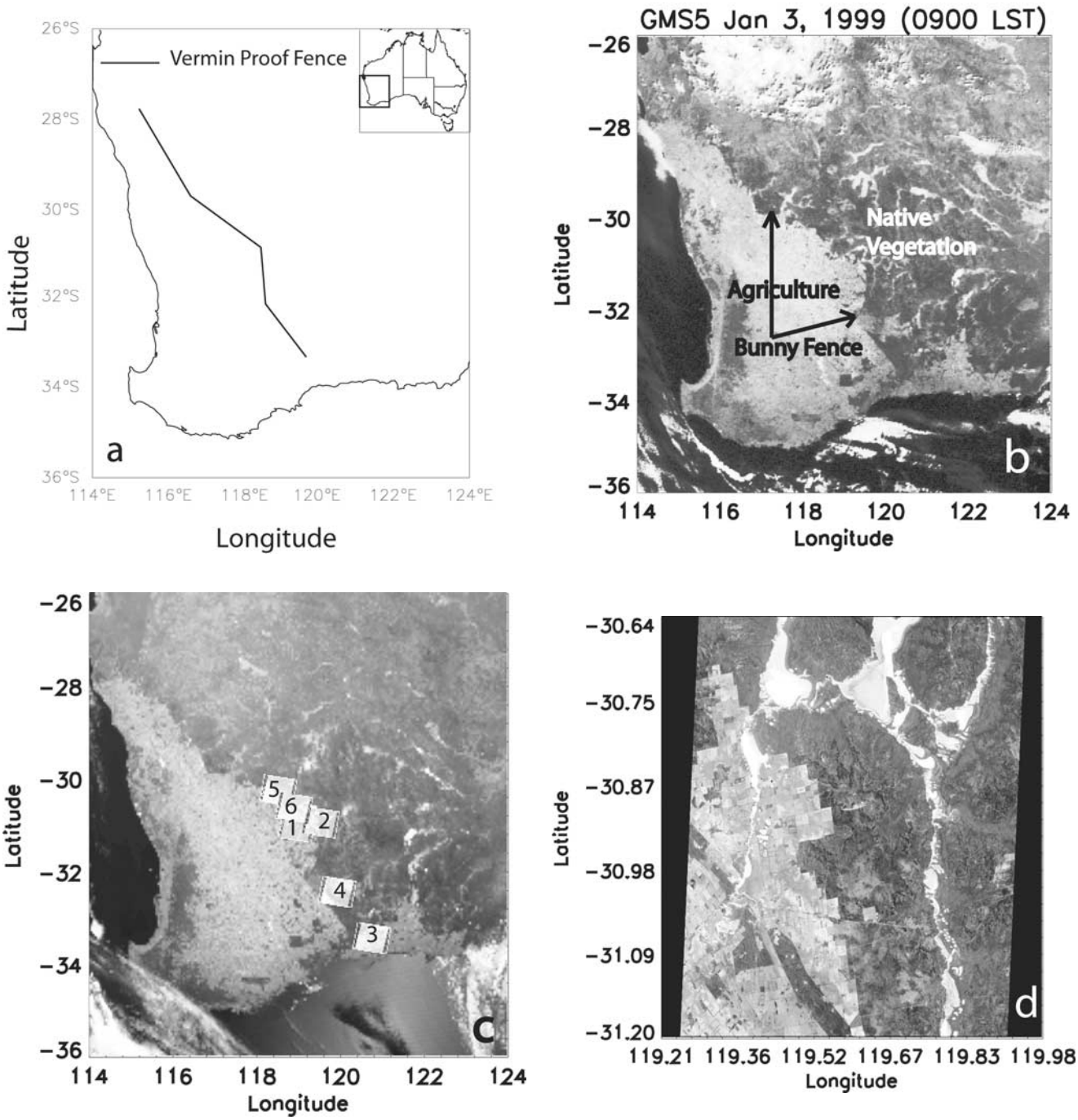

Figure 1. (a) Region of study over Southwest Australia. (b) Geostationary Meteorological Satellite-5 channel 1 imagery over Southwest Australia showing the location of the region of study. (c) Collocated MODIS and the six ASTER images used in this study over Southwest Australia (see Table 1 for details about the ASTER images). (d) ASTER image number 2 showing the detailed nature of the vermin fence in this area.

soil moisture fraction (defined as the ratio of the soil water content to that at field capacity) and surface energy fluxes.

[11] Three different satellite data sets are used in this study, as briefly described below.

2.1. Advanced Spaceborne Thermal Emission and Reflection Radiometer (ASTER)

[12] ASTER data is used in conjunction with the SVAT model [*Gillies et al.*, 1997] for the retrieval of fractional soil moisture availability and surface energy fluxes. ASTER views the Earth in 14 bands ranging from the visible to the thermal infrared. Spatial resolutions vary from 15 m for the visible and near-infrared channels (channels 1–3), 30 m for the shortwave infrared channels (channels 4–9), and 90 m for the thermal infrared channels (channels 10–14). For the retrieval of fractional soil moisture availability and surface energy fluxes, visible channel 2 (0.63–0.69 μm) and near-infrared channel 3 (0.76–0.86 μm), as well as the

Table 1. Dates and Times of the Six ASTER Images Used in This Study

ASTER Image Number	Date	Time, LT
1	Sept. 17, 2000	1031
2	Nov. 4, 2000	1029
3	Nov. 22, 2000	1018
4	Dec. 15, 2000	1023
5	Dec. 22, 2000	1029
6	Jan. 16, 2001	1022

atmospherically corrected surface radiant temperature from channel 14 (10.95–11.65 μm), are used. Since the ASTER duty cycle has been severely limited by the NASA Earth Observation System (EOS) project, the number of ASTER scenes available for this study is limited.

2.2. Geostationary Meteorological Satellite-5 (GMS5)

[13] The GMS5, positioned at 140°E, provides hourly coverage of Southwest Australia from which daytime images of time period 0800 to 1500 LT are used in this study. GMS5 is the latest satellite in the GMS series and was launched in March 1995. It has four channels, three in the infrared and one in the visible (0.5–0.75 μm) wavelength. The spatial resolution for the visible channel is 1.25 km [*Su et al.*, 2000]. GMS5 visible channel data from January 1999 to December 2000 are used to detect cumulus clouds over Southwest Australia.

2.3. Moderate Resolution Imaging Spectroradiometer (MODIS)

[14] For the determination of visible channel reflectance, Normalized Difference Vegetation Index (NDVI), land surface temperature, and cumulus cloud optical properties across the vermin fence, and MODIS satellite data spanning the months of August 2000 to December 2000 are used. MODIS has a swath width of 2330 km and views the surface of the Earth in 36 spectral bands, sampling the electromagnetic spectrum from 0.4 to 14 μm with spatial resolutions ranging from 250 to 1000 m. For the determination of cloud optical properties, bands 1 (0.62–0.67 μm), 20 (3.66–3.84 μm), and 31 (10.78–11.28 μm) are used at a spatial resolution of 1 km. For the determination of NDVI bands 1 and 2 (0.84–0.88 μm) are used. The MODIS cloud mask and land surface temperature products also are used in this study.

3. Methodology

[15] Soil moisture fraction availability and surface energy fluxes over agricultural and native vegetation areas in Southwest Australia are retrieved using ASTER satellite data in conjunction with the SVAT model. The SVAT model has standard errors of 25–55 W m^{-2} in surface energy flux estimation and 16% for fractional soil moisture availability estimation, as determined during field experiments in Kansas and Arizona [*Gillies et al.*, 1997].

[16] The cloud detection technique used in this investigation specifically targets boundary layer cumulus cloud fields, which in general are strongly coupled to local surface processes. Varying surface conditions on the two sides of the bunny fence should result in different cumulus cloud fields, but not upon large-scale frontal cloudiness. The cloud detection scheme used in this study is effective in eliminating the larger cloud systems associated with frontal activity. However, it should be noted that it is impossible to completely eliminate the influences of frontal activity from this analysis.

[17] In order to determine preferential formation and properties of cumulus clouds, accurate detection of the cumulus clouds is of vital importance. The automated Structural Thresholding algorithm [*Nair et al.*, 1999, U. S. Nair et al., Detection of boundary layer cumulus cloud fields in GOES satellite imagery, submitted to *Journal of Applied Meteorology*, 2002, hereinafter referred to as Nair et al., submitted manuscript, 2002] is used for identifying cumulus cloud pixels. It has an accuracy of about 93% [*Nair et al.*, 1999, also submitted manuscript, 2002]. Cumulus cloud pixels identified from GMS5 visible images are used to create diurnal maps of monthly frequency of occurrence of cumulus clouds at eight hourly periods for 1999 and 2000 (0800–1500 LT). Cumulus cloud pixels identified from MODIS images are used for computing cumulus cloud properties at the time of overpass (roughly 1030 LT) for August–December 2000. The method of determining cumulus cloud properties uses a lookup table approach of precalculated radiances from a radiative transfer model [*Han et al.*, 1994].

3.1. Determination of Available Soil Moisture Fraction and Surface Energy Fluxes

[18] The triangle method developed by *Gillies and Carlson* [1995] and *Gillies et al.* [1997] is used to estimate available soil moisture and surface energy fluxes using satellite data in conjunction with the SVAT model. The triangle method is based on the interpretation of observed triangular shape in a scatterplot between satellite-derived NDVI values and surface radiant temperatures. NDVI is defined as:

$$\mathrm{NDVI} = (\alpha_{\mathrm{NIR}} - \alpha_{\mathrm{Red}})/(\alpha_{\mathrm{NIR}} + \alpha_{\mathrm{Red}}), \quad (1)$$

where α_{NIR} (ASTER channel 3; MODIS channel 2) and α_{Red} (ASTER channel 2; MODIS channel 1) are the near-infrared and red surface albedo, respectively. *Gillies et al.* [1997] proposed that the triangular shape observed in such a scatterplot is due to the physical characteristics imposed by limits on distribution of soil moisture and fractional vegetation cover. At low vegetation cover (low NDVI), a given range of soil moisture values causes a wide variation in the range of surface radiant temperature. However, at higher fractional vegetation cover (higher NDVI) the range in variation of surface radiant temperature decreases due to

Table 2. Names and Locations of Stations From Which Radiosonde Data Were Obtained for This Study

Station Name	Latitude	Longitude
Geraldton Airport	−28.78	114.70
Kalgoorlie Boulder	−30.77	121.45
Perth International/Belmont	−31.93	115.95
Esperence	−33.82	121.88

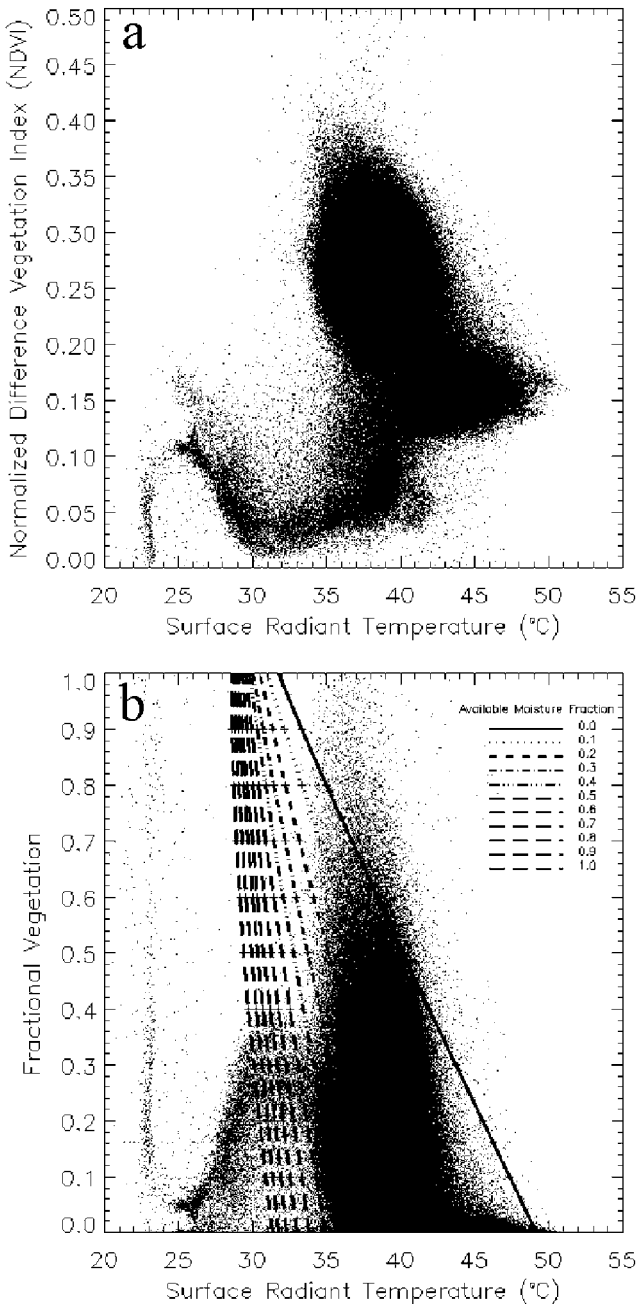

Figure 2. (a) Scatterplot of NDVI versus surface radiant temperature shows a characteristic triangular pattern. (b) Simulated model triangle together with the scatterplot shows a high degree of overlap.

modulation of surface energy fluxes by vegetation. The scatterplot of NDVI and surface radiant temperature values (Figure 2a) derived from the ASTER image shown in Figure 1d shows this characteristic triangular pattern with the range of surface radiant temperature variation decreasing with increasing values of NDVI. The points along the edge on the right side of this triangle correspond to pixels with low soil moisture and thus low surface moisture availability, while the points along the edge on the left side corresponds to pixels with high soil moisture content and hence high surface moisture availability.

[19] For specified atmospheric conditions, the variation of surface radiant temperatures and surface energy fluxes can be simulated for a range of surface moisture availabilities (0–1.0) and fractional vegetation covers (0–1.0) using the SVAT model. If the SVAT-simulated range of surface radiant temperatures matches the satellite observations of same as function of fractional vegetation cover, then for given values of surface radiant temperature and fractional vegetation cover, the surface moisture availability and energy fluxes can be inverted from the model-simulated values. The satellite-observed NDVI can be related to fractional vegetation cover (Fr) as $Fr = N^{*2}$, where N^* is the scaled NDVI given by:

$$N^* = (\mathrm{NDVI} - \mathrm{NDVI}_l)/(\mathrm{NDVI}_h - \mathrm{NDVI}_l) \qquad (2)$$

where NDVI_l and NDVI_h are NDVI values at the base and the top (Figure 2a) of the triangular shaped scatter, in the NDVI-T_{rad} scatterplot.

[20] The SVAT model requires atmospheric information such as temperature, dew point temperature, pressure, height, wind speed, and direction as inputs. Radiosonde data are used for this purpose. Surface characteristics such as soil and vegetation properties are prescribed. The SVAT model-simulated T_{rad} values as function of Fr are used for inferring surface moisture availability from satellite observations. The SVAT model is initialized with atmospheric conditions (closest to the time of satellite overpass, around 1000 LT) from the radiosonde station (Table 2) closest to the satellite scene, and the surface vegetation and soil characteristics that are applicable for the region. The SVAT model is then used to simulate T_{rad} and energy fluxes for discrete values of surface moisture availability and Fr ranging from 0 to 1 in increments of 0.1. The moisture availability associated with a pixel is obtained by comparing the satellite observations of T_{rad} and Fr to the model-simulated triangle for the scene. For atmospheric conditions associated with area shown in Figure 1d and for discrete values of soil moisture availability ranging from 0 to 1 in increments of 0.1, the SVAT model-simulated values of T_{rad} as a function of Fr are shown in Figure 2b. Also, overlaid on this plot are the satellite-observed values of T_{rad} and Fr derived from satellite-observed NDVI values. Notice that there is a very good correspondence between the satellite observations and the model-simulated surface radiant temperature patterns. For Fr values close to zero, model-simulated values of T_{rad} range from about 32° to 48°C. Note that the satellite-observed range of T_{rad} values for pixels with near-zero Fr values are similar. When the surface moisture availability is low, the model simulation shows large variations in T_{rad} with Fr. However, when the surface moisture availability is high, the variation of T_{rad} with Fr is relatively small. For example in Figure 2b, if the satellite-observed values of T_{rad} and Fr are 35°C and 0.6, then the SVAT-simulated triangle shows that the moisture availability is between 0.1 and 0.2. To determine the exact values of moisture availability, interpolations using polynomial fits to SVAT-simulated values are used.

[21] The SVAT model also computes surface energy fluxes (sensible and latent heat fluxes) at discrete values of moisture availability and Fr. An interpolation procedure, similar to the one used for determining moisture availability,

is used for inverting the surface energy fluxes from satellite observations.

3.2. Cumulus Cloud Detection and Statistical Analysis

[22] The Structural Thresholding method of cumulus cloud detection uses the spatial structure of the cloud elements in a scene to determine the location of cumulus clouds [*Nair et al.*, 1999, also submitted manuscript, 2002]. Once cumulus cloud pixels are identified in each of the GMS5 images, the monthly frequency of occurrence of cumulus clouds over agricultural and native vegetation areas are computed from 0800 to 1500 LT at hourly intervals. Cumulus clouds similarly are detected in MODIS imagery, from which cloud properties are retrieved.

3.2.1. Cumulus Cloud Detection From GMS5 Images

[23] The Structural Thresholding algorithm uses cloud number density (number of clouds per unit area) as a discriminant for identifying cumulus clouds. The method consists of three steps, as described below.

[24] The first step consists of subtracting the background albedo from the visible imagery to yield contrast-enhanced images. In the second step, a region growing algorithm [*Levine and Shaheen*, 1978; *Chou et al.*, 1994; *Nair et al.*, 1999, also submitted manuscript, 2002] is used to identify cloudy pixels within the visible channel imagery. The application of region growing algorithm assigns pixels to unique pixel clusters. The mean gray levels of the clusters then are used to threshold the cloudy pixels from the background. *Nair et al.* [1999, also submitted manuscript, 2002] found that cloudy pixels are members of clusters that have a contrast-enhanced mean value of 30 or more. Thus pixels in the enhanced visible channel imagery belonging to clusters whose mean value exceeds 30 are flagged as cloudy pixels.

[25] The third step involves detection of cumulus cloud fields and individual cumulus clouds, which is accomplished by analyzing the spatial structure of the cloud field. Cloud number density is used as a discriminant to identify cumulus cloud fields. To determine the cloud number density, the segmentation technique of *Kuo et al.* [1993] is applied where unique identifying numbers are assigned to pixels belonging to the same cloud. The segmentation algorithm also calculates the location of the individual cloud centroid. Details are given in the work of Nair et al. (submitted manuscript, 2002).

3.2.2. Cumulus Cloud Detection From MODIS Images

[26] The cumulus cloud detection technique from MODIS scenes is similar except for the creation of the all-water cloud mask. In the first step the Interactive Visualizer and Image Classifier for Satellites (IVICS) [*Berendes et al.*, 2001] software is used to classify a MODIS scene and identify all the water clouds. IVICS is a general-purpose visualization and cloud classification system, which supports several types of satellite data, including MODIS. The classifiers were trained with samples selected using IVICS [*Berendes et al.*, 2001]. A cloud mask of the IVICS-identified water clouds is created in the second step. In the third step, cloud segmentation is performed on the cloud mask to identify cumulus clouds within the MODIS scene.

3.2.3. Cumulus Cloud Occurrence Statistics From GMS5 Visible Imagery

[27] Once cumulus clouds are detected from individual GMS5 visible imagery, monthly maps of the frequency of occurrence of cumulus clouds, for hours ranging from 0800 to 1500 LT, are created. The frequency of occurrence of cumulus clouds is simply the number of times a pixel is flagged as a cumulus cloud for a particular hour of the day in a month. This value is then converted to a percentage, 100% indicating that the pixel was flagged as a cumulus cloud each day of the month for that particular hour.

3.3. Determination of Cumulus Cloud Properties

[28] MODIS images spanning the months of August 2000 to December 2000 were used to determine cumulus cloud optical and microphysical properties. The harvesting of wheat and barley crops over agricultural areas continues until the beginning of October, after which the agricultural areas remain barren, whereas the native vegetation continues to transpire. Therefore by studying the cumulus cloud properties from August to December, the entire seasonal trend of agricultural to barren ground is captured.

3.3.1. Retrieval of Cumulus Cloud Properties

[29] The retrieval scheme for cumulus cloud properties consists of generating lookup tables of precalculated radiances from a radiative transfer model, which relates the satellite observations in the three MODIS channels to cloud particle size and optical thickness. All retrievals are conducted for those pixels that are determined to be cloudy by the cloud mask described in section 3.3.2. Cloud properties were retrieved for all liquid water clouds, determined by cloud top temperature $T_C > 273.2$ K. However, the present study is limited to cumulus clouds.

[30] Four lookup tables are created. The first lookup table is a first guess value of the thermal emission contribution to 3.7 μm radiances. This first guess value is obtained using cloud optical thickness (τ) from the visible band reflectance, assuming the value of cloud mean effective radius (r_e) as 10 μm, and using the thermal radiance of MODIS channel 31 and the surface temperature (T_S) as entries. Because the cloud thermal emission also is a function of cloud particle size, the assumed value of 10 μm is used as the first guess and then iterated as improved values of r_e become available. Subtracting the estimated thermal emission from the total 3.7 μm radiance, we obtain the reflected solar radiance in the 3.7 μm radiance.

[31] The second lookup table removes the effect of solar radiation reflected from the surface to isolate the cloud reflectance at 3.7 μm. The magnitude of this effect depends on the cloud optical thickness. The table's inputs are cloud optical thickness (τ), cloud particle effective radius (r_e = 10 μm as a first guess), surface reflectance for the 3.7 μm band (R_S), cosine of the solar zenith angle (μ_0), viewing zenith angle (μ), and relative azimuth angle (ϕ). Surface reflectance for a specific location is the monthly mean value derived from 3.7 μm measurements in clear pixels.

[32] The third lookup table gives the cloud particle size, r', using entries for reflected solar radiance at 3.7 μm, the initial cloud optical thickness (τ_o), the cosine of the solar zenith angle (μ_0), and the water vapor amount above the cloud (w) from Television Infrared Observation Satellite (TIROS) Operational Vertical Sounder (TOVS) and the cloud top pressure. The new value of cloud droplet radius (the second guess) is entered into the fourth table to obtain an improved estimate of the cloud thermal emission at

3.7 μm. The fourth table is similar to the first table. If the difference between this new value and the previous (or first) guess is larger than certain threshold (about 0.5 K), we subtract the new value of the thermal emission contribution from the 3.7 μm radiance and repeat the whole particle size retrieval. This process continues until the thermal emission contribution converges. Then $r_e = r'$ is the effective radius for $\tau = \tau_0$.

[33] Next, the effect of particle size on cloud optical thickness is accounted for by an iterative calculation that includes changes in cloud optical thickness in the retrieval. According to radiative transfer theory [e.g., *Van de Hulst*, 1980; *Twomey et al.*, 1984], two cloud layers have about the same reflection, transmission, and absorption properties if they have the same values for a scaled optical thickness and scaled single-scattering albedo (ϖ_o). Therefore the similarity equation,

$$\tau'(1 - \varpi_o' g') = \tau(1 - \varpi_o g), \tag{3}$$

is used to obtain τ' from τ and r' [note that ϖ_o and g (asymmetry factor) are functions of wavelength (λ) and droplet radius, and are calculated using Mie theory and the optical constants of liquid water instead of using the scaling equations for these quantities]. If the difference of τ' and τ is greater than a threshold value, the fourth lookup table is used again to obtain a new thermal emission contribution to the 3.7 μm radiance and the whole r_e retrieval repeats until τ converges (the calculation of the surface effect also is repeated in each iteration).

[34] The primary consideration in choosing convergence criteria for τ is computer time and the magnitude of errors. The iterative process is terminated if the difference of retrieved particle sizes in two successive cycles is $|r' - r_e| \leq 1$ μm (which is within the estimated accuracy of the retrieval scheme) and $|\tau' - \tau| < 0.1$. With these criteria, the data processing speed and the errors are satisfactory [*Han*, 1992]. Details of sensitivity tests, verification efforts, and error estimations of this algorithm are discussed by *Han et al.* [1994, 1995].

[35] Cloud liquid water path (LWP) is computed from the retrieved cloud optical thickness and effective radii using the equation

$$\mathrm{LWP} = (2/3)\tau(\lambda)\rho_w r_e, \tag{4}$$

where ρ_w is the density of liquid water. Water cloud optical and microphysical properties are retrieved in this manner from all MODIS images spanning the months August 2000 to December 2000. In the next step MODIS images free from large frontal clouds are selected, by visually inspecting three band overlays of all the images. These images are used for retrieving mean cumulus cloud properties over agricultural and native vegetation areas.

4. Results

[36] The Southwest Australian region under consideration (114°–124°E and 26°–36°S in Figure 1) has a Mediterranean type of climate. In the winter rainy season, wheat and barley crops are grown in the agricultural areas, whereas during the dry summer season the agricultural areas are left barren. The agricultural areas are separated from the perennial native vegetation areas by the vermin fence, which sharply divides both the vegetation types. Seasonal differences in land surface properties such as land surface temperature, visible channel albedo, NDVI, available soil moisture fraction, and surface energy fluxes are observed between these two juxtaposed regions. Seasonal differences in the frequency of occurrence of cumulus cloudiness and cumulus cloud properties over the two vegetation types also are clearly discernable and appears to be influenced by the nature of land use.

4.1. Observation of Land Surface Temperature, Channel 1 Albedo, and NDVI

[37] Figure 3a shows the monthly variation of land surface temperature averaged over agricultural and native vegetation areas using cloud-free MODIS data at 1030 LT. In the agricultural months of August (Julian days 212–243) and September (Julian days 244–273) the land surface temperature is similar over both the vegetation types. It averages as 292 and 291 K over agriculture and native vegetation areas, respectively, in August. In September the average values are 297.6 and 298.8 K, respectively. As the summer season progresses from October to December, land surface temperature rises over both the vegetation types, but the agricultural areas warm considerably more than the native vegetation areas. In December, the land surface temperature averages 320.2 K over agricultural areas and 316.6 K over native vegetation areas. Thus the agricultural areas tend to be about 3.6 K warmer than native vegetation areas at this time of the year. Land surface temperatures derived from the high-resolution ASTER images also show similar differences in temperatures between the two vegetation types. The observed gradient in land surface temperatures is very sharp across the bunny fence.

[38] Channel 1 albedo values (0–1) determined from MODIS images show slightly higher average values of 0.13 over agricultural areas, compared to 0.10 over native vegetation areas during August (Figures 3b and 3d). In comparison, *Lyons* [2002] reports albedo values of 0.18 and 0.08 for agricultural and native vegetation areas during August, respectively. After the harvesting of agricultural crops, which takes place by the beginning of October in this region, the agricultural areas are left barren. Average albedo values keep on increasing over both the vegetation types during the dry summer season, reaching values of 0.20 over agricultural areas by December, whereas over native vegetation areas it increases marginally to 0.11. In comparison, *Lyons* [2002] reports values of 0.27 and 0.12 for albedo values over agricultural and native vegetation regions in December, respectively. This results in a sharp gradient in channel 1 albedo values between agricultural and native vegetation areas during the summer (Figure 3e). Monthly maps of channel 1 albedo for August through December clearly show the seasonal changes and the development of the albedo gradient between agricultural and native vegetation areas. Sharp gradient in visible channel albedo also is present in the ASTER images.

[39] Monthly average values of NDVI determined from MODIS images over Southwest Australia from the months of August 2000 (winter season) to December 2000 (dry season) also show similar seasonal changes over the two

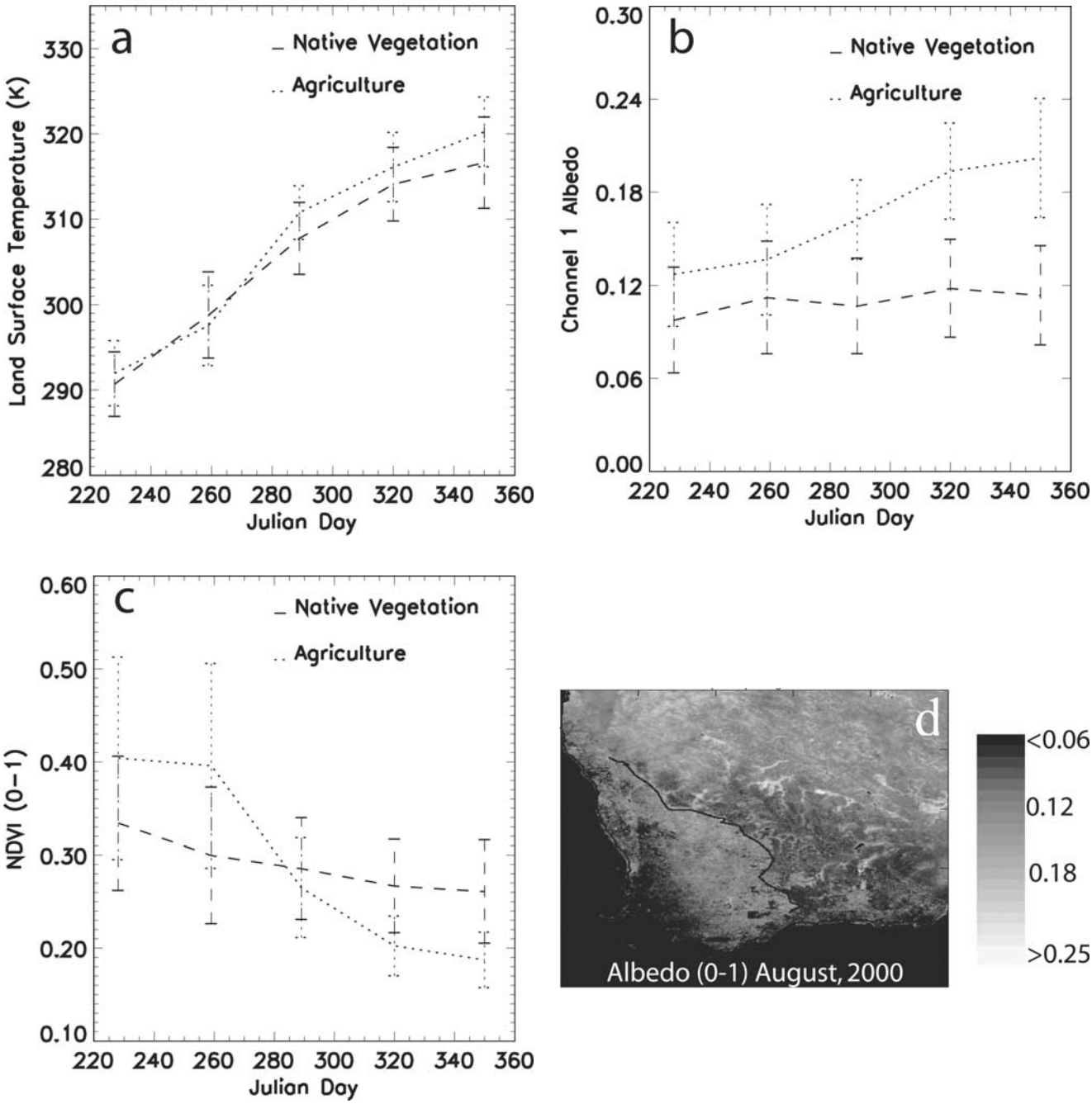

Figure 3. Seasonal variation of (a) land surface temperature, (b) channel 1 albedo, (c) NDVI, (d) NDVI image in August, (e) NDVI in December, (f) channel 1 reflectance in August, and (g) channel 1 reflectance in December.

vegetation types (Figure 3c). In August, NDVI values are higher over agricultural areas with an average of 0.40. Over native vegetation areas the average value in August is 0.33. The corresponding regional maps are shown in Figures 3f and 3g. The NDVI values then decrease to 0.26 over agricultural areas and to 0.29 over native vegetation by October. By December the NDVI average values over agricultural areas are only 0.19, whereas over native vegetation areas the average values are 0.26. Therefore over agricultural areas NDVI values decrease by a factor of 2 between the wet and dry seasons, whereas for native vegetation there is only a moderate decrease in NDVI values during the dry season.

4.2. Surface Energy Fluxes and Available Soil Moisture Fraction

[40] The soil moisture availability retrieved from ASTER imagery (Figure 4a) shows the sharp decrease in moisture availability (0–1) from winter to summer over both the vegetation types. Values of about 0.4–0.5 are found during winter, decreasing to values of 0.05–0.1 in summer over agriculture and native vegetation, respectively. The seasonal

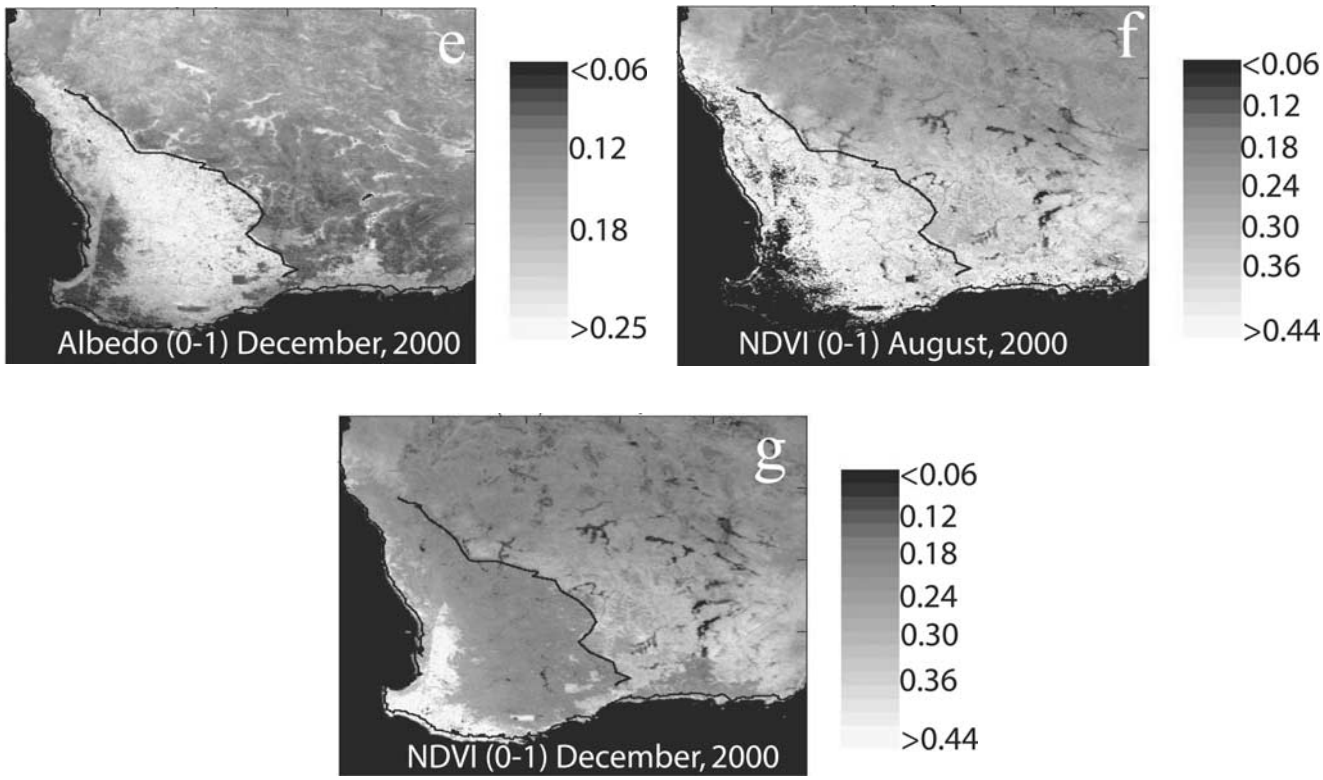

Figure 3. (continued)

fractional moisture availability is higher over agricultural areas during winter. During dry summer season both areas have almost similar available soil moisture fractions.

[41] Figure 4b shows that the ASTER retrieved sensible heat flux increases rapidly from winter to summer over both agricultural and native vegetation areas as the incoming solar energy increases but with major differences. In the agricultural season month of September, sensible heat fluxes are about the same over native vegetation and agricultural areas. However, for the dry summer months of October–December, sensible heat fluxes are higher over agricultural areas. During December sensible heat fluxes are on average about 31 W m^{-2} higher over agricultural areas. Figure 4c shows that the magnitude of the latent heat fluxes over agricultural and native vegetation areas are similar in the month of September during harvest. Immediately after harvest these differences can be as large as 150 W m^{-2}, decreasing to about 50–70 W m^{-2} during the summer months. During the months of October to December, with the absence of vegetation over agricultural areas, the bare soil dries rapidly, leading to decreasing available soil moisture and hence a corresponding decrease of latent heat fluxes. Native vegetation continues to transpire but at a lower rate during the hot summer months, with the result that latent heat fluxes are significantly higher over native vegetation.

[42] The pixel-by-pixel variation of various surface characteristics along a line oriented east to west on ASTER data for 4 November 2000 (Figure 5a) shows sharp discontinuities between agricultural and native vegetation areas. Figure 5b shows that channel 1 reflectance is variable but averages about 0.13 over the agricultural regions and about 0.08 over native vegetation. Notice the sharp break at the boundary. The presence of such a sharp boundary suggests that adjacency effects are not important in this area. Likewise, Figure 5c shows values of surface temperature. Over agricultural regions surface temperatures range from about 40° to about 50°C with mean value of about 45°C, whereas over native vegetation mean temperature is about 38°C. Note in particular that temperature drops almost 10°C at the boundary over a distance of several hundred meters. Figure 5d shows that the NDVI values over the relatively barren agricultural regions average to about a value of 0.16 and to about 0.28 over the native vegetation. These values are similar to that found in the MODIS data (see Figure 3c); however, the NDVI values for barren agricultural areas shown in Figure 5d are smaller than those found in the MODIS results. The MODIS results are averaged over large (several thousand km^2) regions that are not homogeneous and that likely have some areas other than barren soil. Figure 5e shows values of moisture availability. Values range from about 0.15 to more than 0.5 over agricultural regions, with a mean value of about 0.2. Note the very large change at the boundary with native vegetation. Values of moisture availability range from about 0.2 to nearly 1.0 over native vegetation. Near the boundary, values average about 0.6; however, there are barren sections within the region of native vegetation that are very dry with values similar to those found over agricultural regions. Clearly, neither the agricultural regions nor the native vegetation are homogeneous. Figures 5f and 5g show values of sensible and latent heat flux, respectively. Values of sensible heat flux are approximately 50 W m^{-2}

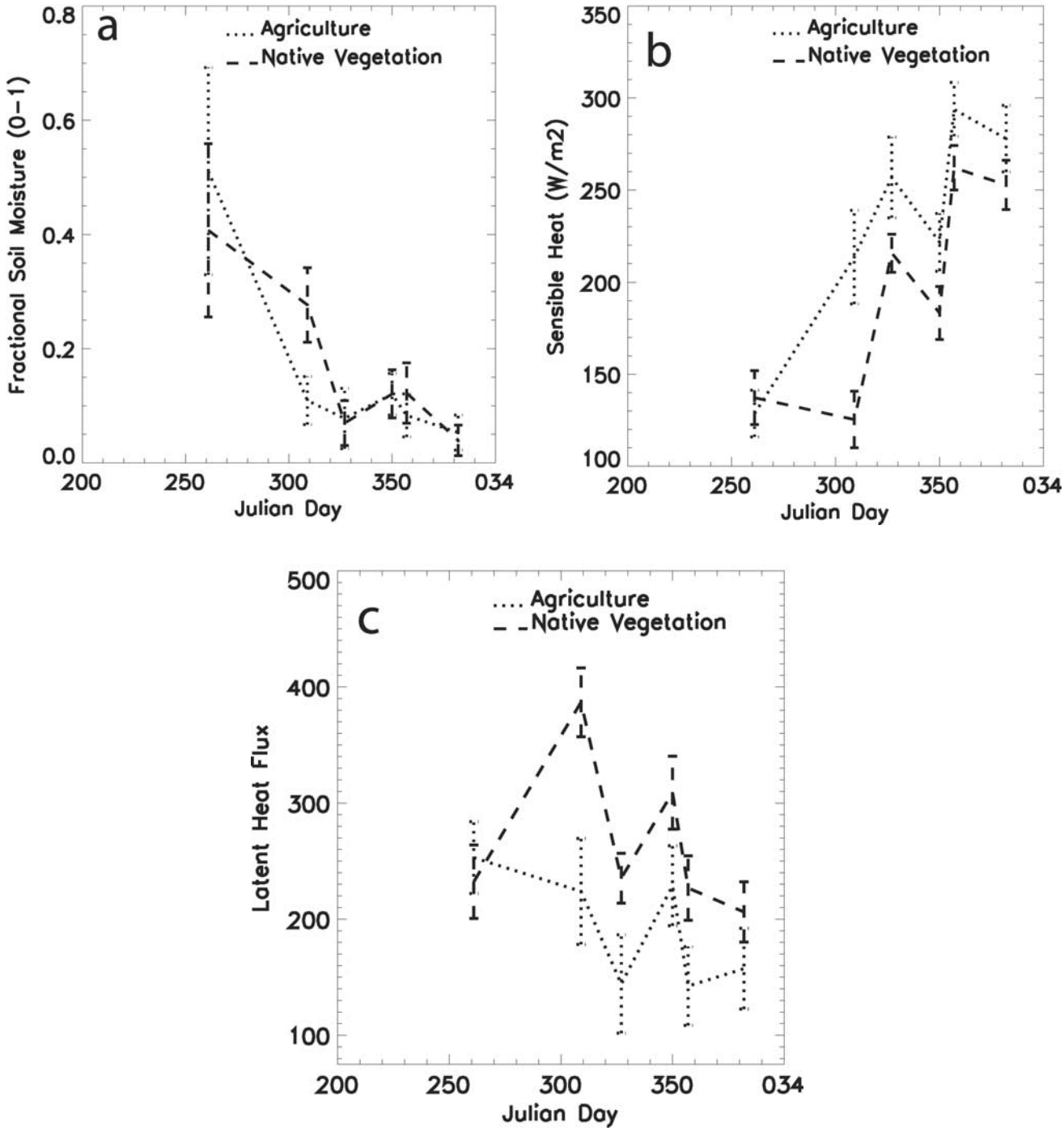

Figure 4. ASTER-retrieved seasonal variation in (a) available soil moisture fraction, (b) sensible heat flux, and (c) latent heat flux.

larger in agricultural regions. Values of latent heat flux are on the order of 200 W m^{-2} over agricultural regions and more than 300 W m^{-2} over native vegetation, once again in rough agreement with values derived from regional averages (see Figure 4c).

4.3. Observations of Cumulus Cloudiness

[43] In order to determine the effect of seasonal changes in land surface properties (as described in section 4.1) on the seasonal pattern of cumulus occurrence, the frequency of occurrence of cumulus clouds over Southwest Australia was computed. The computed frequency is plotted as monthly maps at hourly intervals from 0800 to 1500 LT.

4.3.1. Diurnal Variations

[44] Monthly frequency of occurrence maps generally show an increase in cumulus cloudiness from 0800 to 1500 LT for all months of 1999 and 2000, other than June through August. Figure 6a shows the GMS5 channel 1 image at 0800 LT on 30 August 1999. The agricultural areas to the west of the fence clearly have a much higher

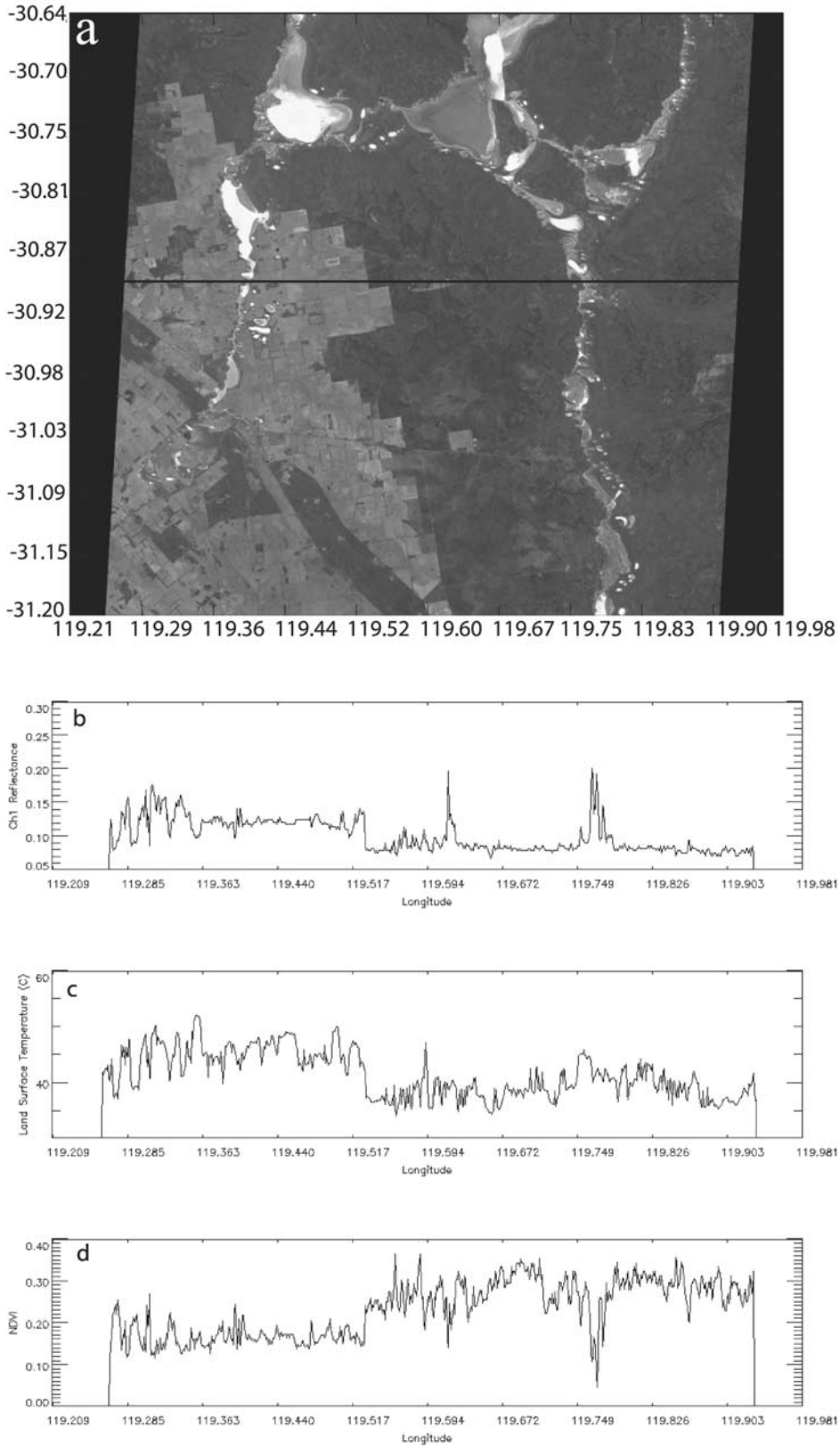

Figure 5. (a) ASTER image from the dry season. Various quantities retrieved along the line drawn across the image were (b) channel 1 reflectance, (c) land surface temperature, (d) NDVI, (e) available soil moisture fraction, (f) sensible heat flux, and (g) latent heat flux.

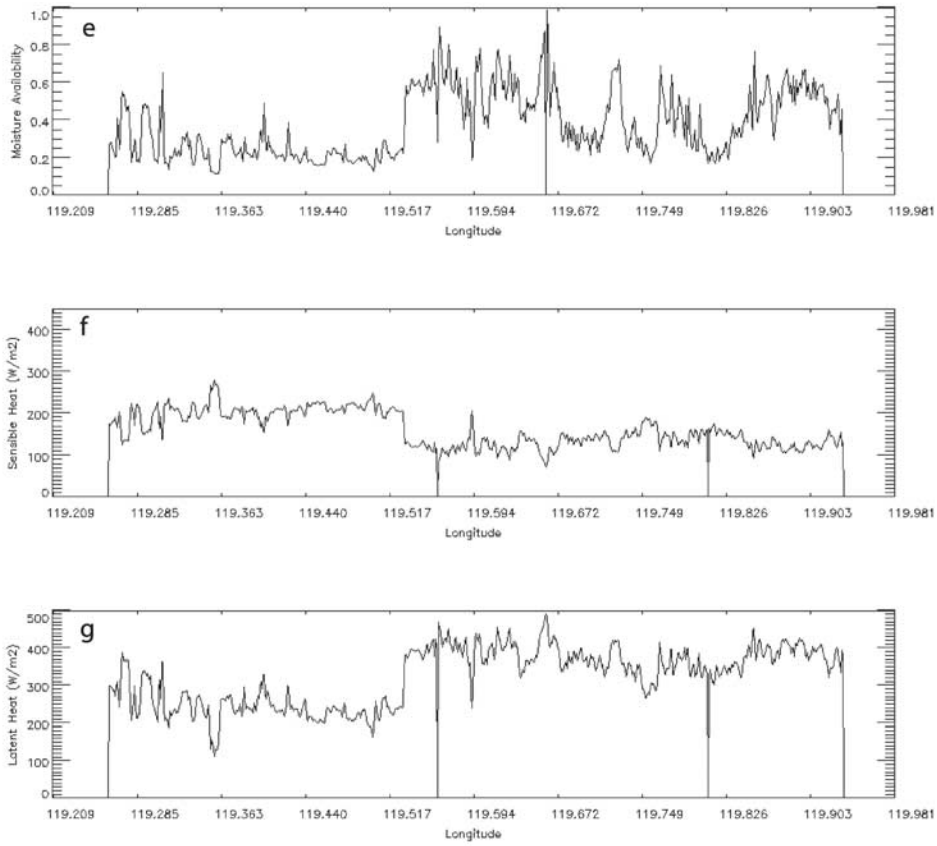

Figure 5. (continued)

albedo than those for native vegetation. Both regions are relatively cloud free at this time. By 1500 LT (Figure 6b), the agricultural areas are almost uniformly covered by shallow cumulus clouds, whereas the region of native vegetation continues to remain cloud free. Figure 6c shows the GMS5 channel 1 image at 0800 LT on 3 January 1999, during the summer. Once again, there is relatively little cloud cover over either region in the early morning hours. However, by 1500 LT cumulus clouds cover nearly all of the native vegetation (Figure 6d), while the barren agricultural areas remain cloud free. There is a complete reversal of cloud cover patterns between August and December–January for the agricultural and native vegetation regions. This clearly demonstrates that land use contributes to the development of cloud cover in these regions. Recall that these regions have no other differences, other than vegetation cover. The differences in topography are small, and there is no evidence of frontal activity in these cases.

[45] Figure 7 shows the frequency of occurrence of cumulus cloudiness for September 2000 at eight different time periods, from 0800 to 1500 LT. At 0800 LT, cloud cover over agricultural regions is significantly higher than over native vegetation. Cumulus cloud cover then keeps increasing over both the regions. Note that the satellite surface property retrievals presented in this investigation correspond to the 1000–1100 LT time period. By 1300 LT cumulus cloud cover is significantly greater over agricultural regions. From 1300 to 1500 LT, cloud cover increases in both agricultural and native vegetation regions, but the increase in cloud cover is much larger over agricultural regions.

[46] During the summer months of December and January, cumulus clouds occur with higher frequency and are spatially more extensive in occurrence over native vegetation during the afternoon hours (Figure 8). Cumulus clouds develop initially in the region close to the vermin fence in the morning hours (during the hours 0800 to 1000 LT). About 1100 LT the region of cumulus cloud formation begins to shift over to native vegetation areas, and it intensifies during the afternoon. The frequency of cumulus cloud occurrence is distinctly higher over native vegetation areas. A careful examination of these 2 months shows a tendency for banking of cumulus clouds at the agriculture-native vegetation junction on the native vegetation side. These results are not inconsistent with *Segal et al.* [1988], *Avissar and Liu* [1996], *Avissar and Schmidt* [1998], and *Weaver and Avissar* [2001] who have shown that differential heating over contrasting surfaces results in the generation of sea-breeze-like mesoscale circulations. Toward late afternoon, 1400–1500 LT, the spatial coverage and frequency of cumulus clouds increase over agricultural areas as well.

4.3.2. Seasonal Variations

[47] Monthly maps of frequency of occurrence of cumulus cloudiness have been generated hourly from 0800 to 1500 LT for 1999 and 2000. While there are differences in the frequency and location of cumulus formation between the years 1999 and 2000, the general seasonal pattern is similar for both years.

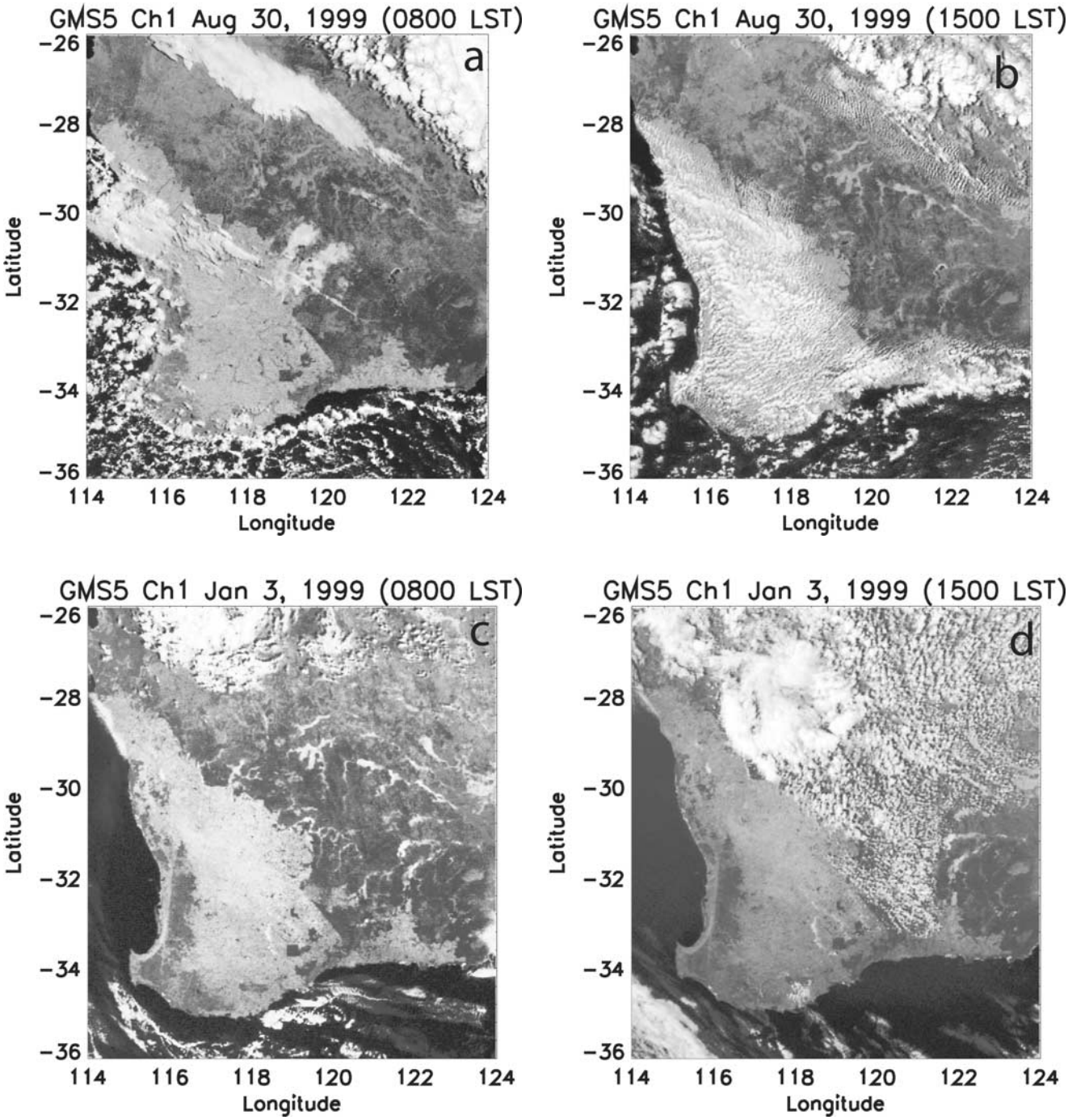

Figure 6. Preferential development of cumulus clouds in Southwest Australia. (a and b) The preferential development of cumulus clouds over agricultural areas from 0800 to 1500 LT during the winter agricultural season. (c and d) The preferential development of cumulus clouds over native vegetation from 0800 to 1500 LT during the summer dry season.

[48] A study of the months of June–September suggests a preferential formation of cumulus clouds over agricultural areas. It also appears that the spatial coverage of cumulus clouds tends to decrease slightly as one moves away from the coast of Southwest Australia. Figure 9 shows the monthly maps of cumulus cloudiness at 1300 LT. It shows that during the summer months of December 2000 and January–March 2000 cumulus clouds occur with higher frequency over native vegetation areas. The interior regions of the barren agricultural areas have lower cumulus cloudiness in these months but those agricultural regions close to the fence have higher cumulus cloudiness. During the winter (agricultural season) months of May–September, cumulus clouds occur more frequently over agricultural areas. In these months the agricultural regions, which had lower cumulus cloudiness in the dry season months now

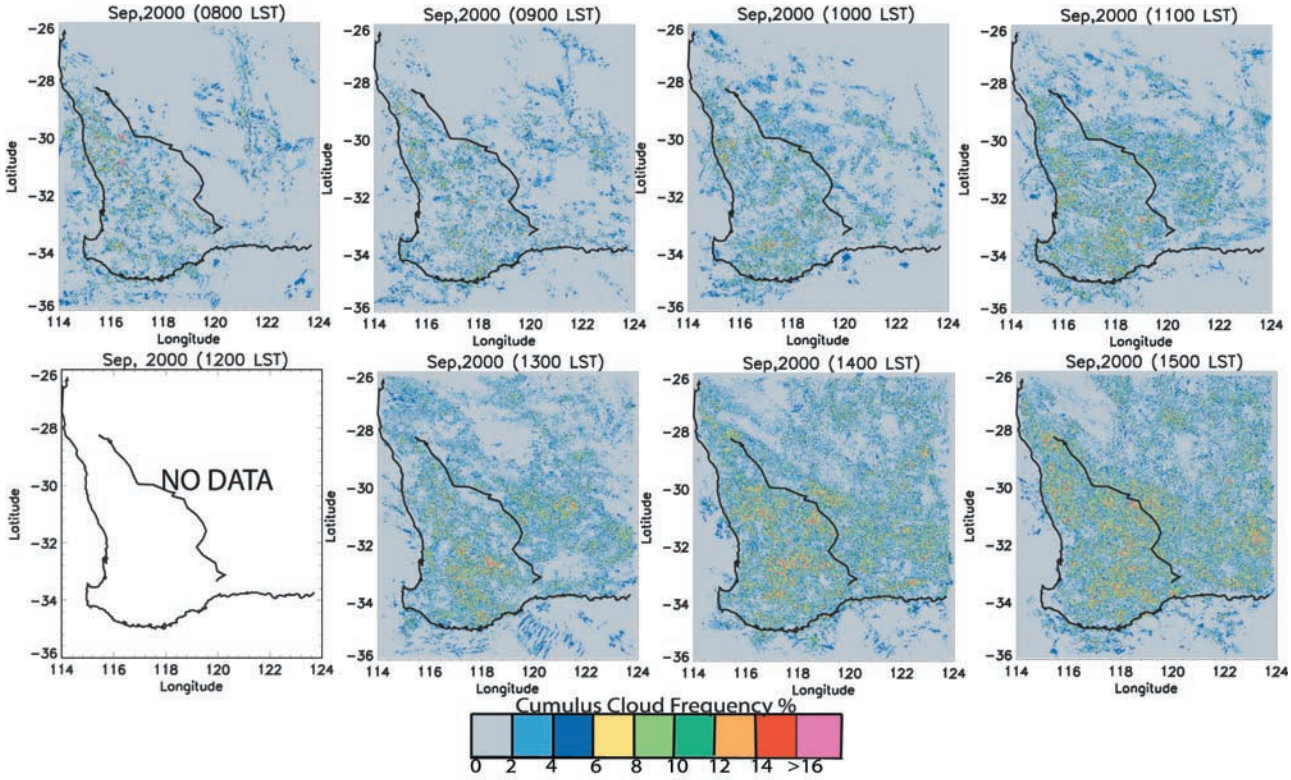

Figure 7. Frequency of occurrence of cumulus cloudiness at 0800–1500 LT for September 2000.

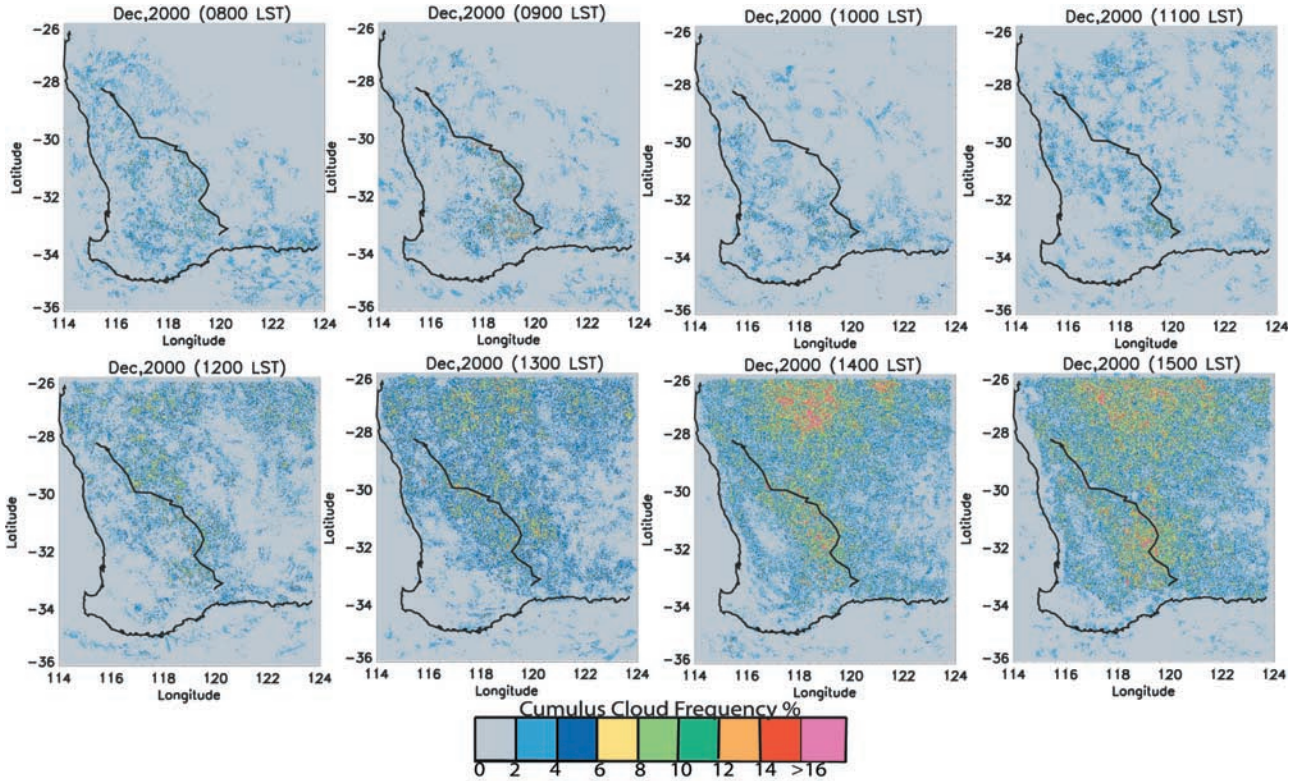

Figure 8. Same as in Figure 7 but for December 2000.

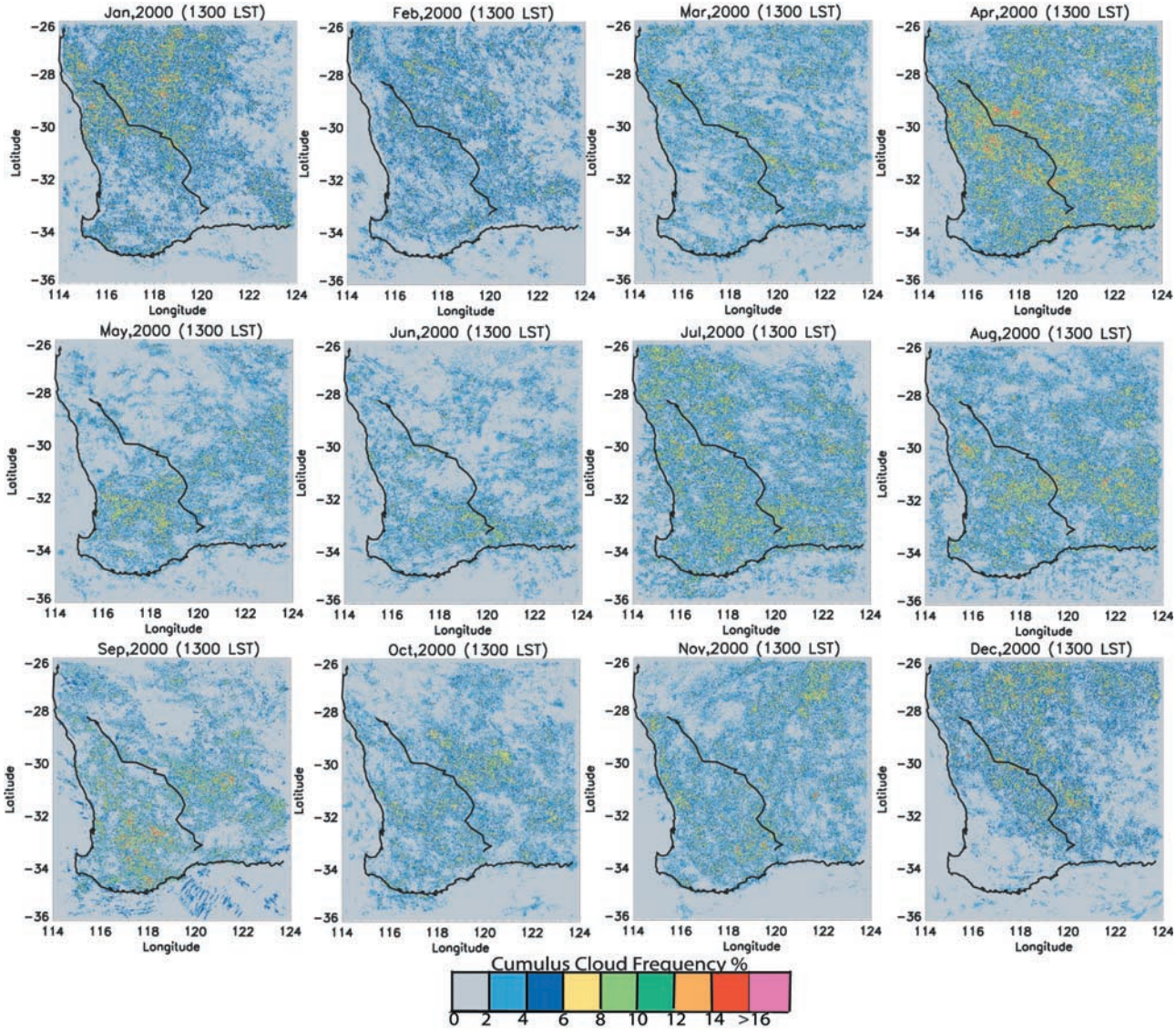

Figure 9. Monthly maps of cumulus cloudiness at 1300 LT for the year 2000. Legend same as in Figures 7 and 8.

have higher values of cumulus cloudiness, whereas the native vegetation areas have relatively lower cumulus cloudiness. This trend clearly shows the effect of land use on cumulus cloudiness. However, winter month frontal systems may also play a role in the spatial distribution of cloudiness.

4.4. Retrieval of Cumulus Cloud Properties

[49] Optical and microphysical properties of cumulus clouds were derived from MODIS images for the months of August to December. In order to study cumulus clouds, which form specifically over agriculture or native vegetation areas, the following precautions were taken. First, cumulus clouds occurring at the edge of large frontally driven cloud systems were rejected, by visual inspection. Second, cumulus clouds close to the vermin fence also were rejected, since they may have been advected across the boundary.

[50] Figure 10a shows that in August at 1030 LT the optical thickness of cumulus clouds over both agricultural and native vegetation areas are similar with typical values of $\tau = 6-7$. However, in September, the optical thickness of cumulus clouds over native vegetation decreases to typical values of $\tau = 5$. During October through December (summer months), the pattern reverses and cloud optical thickness gradually increases to values of $\tau = 8-9$ for native vegetation. Note that cumulus cloud optical thicknesses are relatively constant over agricultural regions for this entire period. Figure 10b shows cumulus cloud LWP (10^{-4} cm) over the two vegetation types. Seasonal differences in cloud LWP are clearly discernable over agricultural and native vegetation areas. During August and September, the LWP is larger over agricultural areas. During the dry season months of October–December the pattern is reversed, with LWP being larger over native vegetation areas. Figure 10c shows the retrieved cumulus

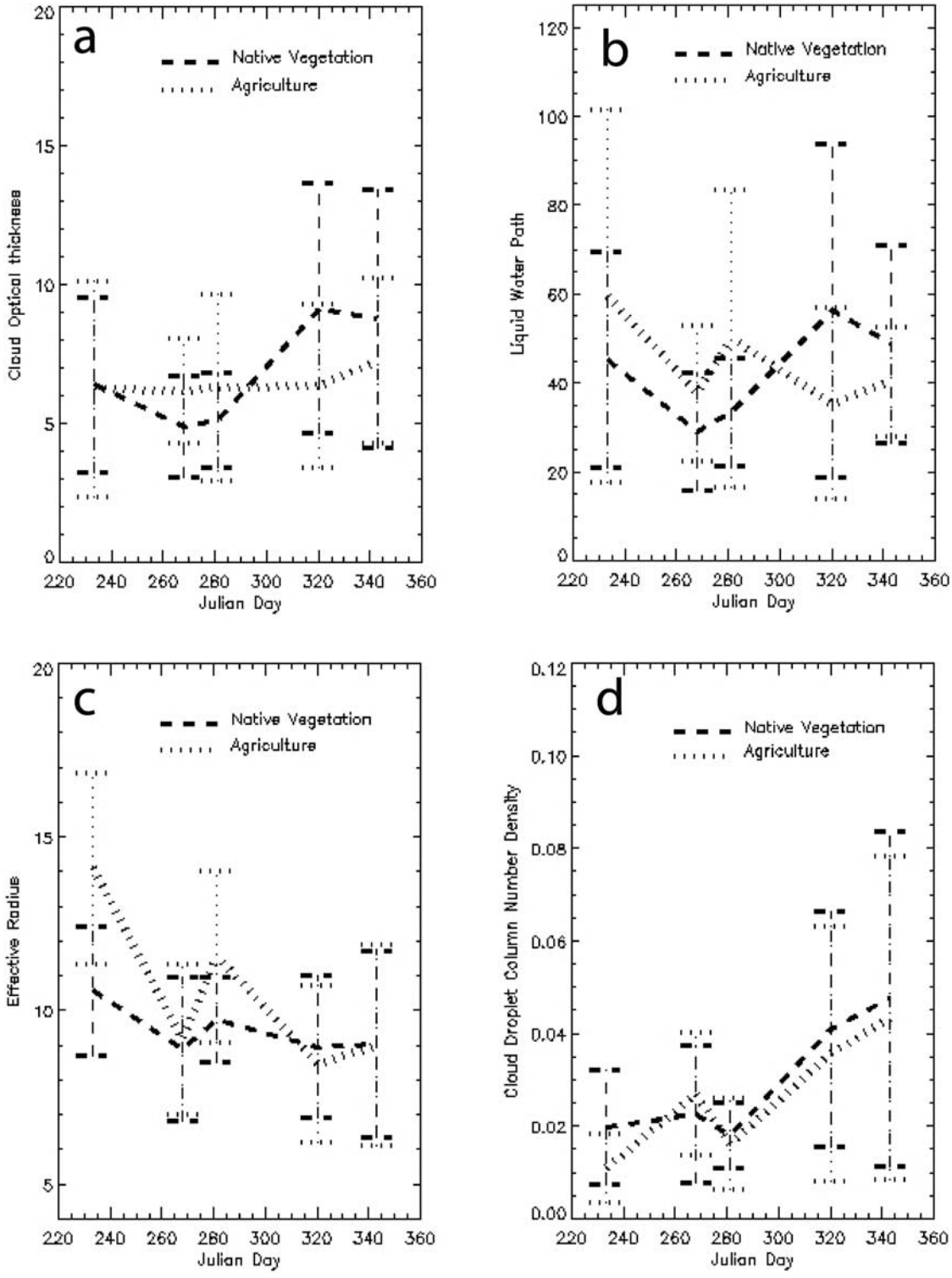

Figure 10. Seasonal variation of cloud optical and microphysical properties. (a) Cloud optical thickness, (b) cloud liquid water path, (c) cloud effective radius, and (d) cloud droplet column number density.

cloud effective radii (μm). The results show that the mean cumulus cloud effective radius is significantly larger over the agricultural areas in the agricultural months of August–September. However, the magnitude of the difference in effective radius over agricultural and native vegetation areas then decreases during the summer months. In December the cumulus cloud effective radius is similar over both areas with values of about 9 μm. Figure 10d shows cumulus cloud droplet column number density (10^8 cm^{-2}) as a function of time. In both agricultural and native vegetation

Table 3. Differences in Average Values of Surface Characteristics and Cumulus Cloudiness Between Agricultural and Native Vegetation Areas for September (Wet Season) and December (Dry Season) at 1000 LT

	August–September		December	
Variable	Agriculture	Native Vegetation	Agriculture	Native Vegetation
Albedo	0.13	0.10	0.20	0.11
Albedo: *Lyons* [2002]	0.18	0.08	0.27	0.12
NDVI	0.40	0.33	0.19	0.26
Surface temperature, K	292	291	320	317
Soil moisture availability	0.51 ± 0.18	0.41 ± 0.15	0.08 ± 0.04	0.12 ± 0.05
Sensible heat flux, W m^{-2}	129 ± 13	137 ± 15	294 ± 15	262 ± 12
Sensible heat flux: Aircraft [1992–1993], W m^{-2}	161 ± 12	209 ± 15	...	...
Latent heat flux, W m^{-2}	253 ± 31	232 ± 32	142 ± 34	227 ± 28
Latent heat flux: Aircraft [1992–1993], W m^{-2}	242 ± 41	226 ± 55	...	...
Monthly mean cumulus cloud cover at 1500 LT, %	5.49	4.20	3.85	6.52

areas, cloud droplet column number densities are similar, but increasing in value during the dry summer months when there is greater dust loading.

4.5. Discussion

[51] The differences in average values of surface characteristics and cumulus cloudiness between agricultural and native vegetation areas for the months of September and December at 1030 LT are summarized in Table 3.

[52] The changes in surface characteristics of the agricultural area, between the month of August and drier summer month of December, is drastic compared to that for the native vegetation area. During this time period, there was a 54% increase in albedo and a 53% decrease in NDVI values over the agricultural area, compared with a 10% increase and a 21% decrease, respectively, for the same over native vegetation. These large differences are associated with harvesting of crops in the agricultural area. The substantial decrease in NDVI values over agricultural areas is due to removal of crop vegetation during harvest, with the subsequent exposure of bare ground resulting in the large increase in surface albedo. Smaller changes in albedo and NDVI over native vegetation areas are due to thinning of vegetation in response to decrease in precipitation during this time period. The patterns of variation in albedo and NDVI between August and December, for both agricultural and native vegetation areas, show qualitative agreement with albedo and NDVI variations reported by *Lyons et al.* [1996] for the same months. Only qualitative comparisons can be made between the present study and the study by Lyons et al., since the albedo and NDVI values reported in the present studies are averaged over large areas, while they are for selected sites in the study by Lyons et al.

[53] In September, the surface soil moisture availability is high for agricultural and native vegetation, but it reduces to significantly lower values for both areas by December. For the months considered in this study, the soil moisture availability generally is higher over native vegetation. *Lyons et al.* [1996] suggest that clearing of native vegetation could be responsible for the recent observed rainfall reduction over agricultural areas. This possible regional climate change brought about by clearing of native vegetation could also be responsible for the observed soil moisture availability differences between agricultural and native vegetation areas.

[54] The percentage decrease in surface moisture availability between the months September and December for agricultural areas (84%) is larger compared to that for native vegetation (71%). Higher losses of moisture from soils in agricultural areas are likely due to enhanced evaporation from surface soils associated with removal of surface vegetation during the harvest.

[55] The harvesting of crops and subsequent exposure of bare ground results in the higher albedos; consequently, the surface energy budgets are considerably different over the agricultural areas during the summer month of December. For the month of September, sensible and latent heat fluxes are approximately equal for both agricultural and native vegetation areas; sensible heat fluxes are 129 and 137 W m^{-2}, respectively, while latent heat fluxes are 253 and 232 W m^{-2}, respectively. Surface temperatures for these areas are also comparable during September (292 versus 291 K).

[56] Aircraft measurements of sensible and latent heat fluxes have been taken on either side of the fence near Lake King from 24 to 30 September 1992 and 4 to 6 October 1993 from 0900 to 1800 LT. The general flight pattern consisted of transects of about 20 km across the agricultural land followed by two transects across the native vegetation (one outbound and one back toward the fence) and then a further transect over the agricultural land. Aircraft heights ranged from about 7 to 95 m. The aircraft measurements have been averaged over 1 hour time periods (Figure 11). Note that over agricultural areas sensible heat fluxes are consistently smaller than latent heat fluxes, with Bowen

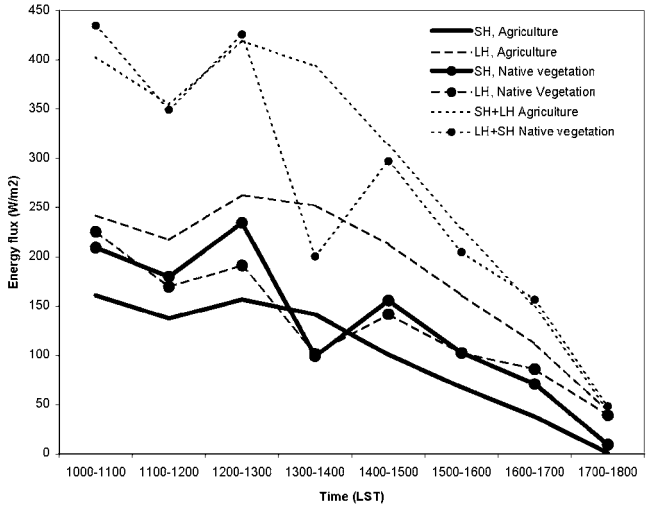

Figure 11. Sensible, latent, and sensible + latent heat flux for agricultural and native vegetation regions averaged over 1-hour intervals from aircraft data for the time period of 24–30 September 1992 and 4–6 October 1993.

ratios of about 1.5–3. On the other hand, note that latent heat fluxes are greater than sensible heat fluxes over native vegetation in the morning (before 1100 LT) and in the late afternoon (after 1600 LT), with Bowen ratios typically just slightly larger than unity. During the heat of the day over native vegetation, the situation reverses, with sensible heat fluxes larger than latent heat fluxes. Corresponding Bowen ratios are about 0.8 to unity.

[57] Aircraft measurements for the time period of 1000–1100 LT are compared with the satellite-derived values taken at approximately 1030 LT (for the year 2000). Comparisons of latent heat values for the satellite and aircraft measurements are in good agreement (253 versus 242 W m^{-2} over agricultural regions and 232 versus 226 W m^{-2} over native vegetation), and the standard deviations are also similar. On the other hand, aircraft-derived sensible heat fluxes are significantly larger (129 versus 161 W m^{-2} over agricultural regions and 137 versus 209 W m^{-2} over native vegetation). The reason for the large discrepancies, especially for the sensible heat fluxes, is unknown. However, note that large variations of latent and sensible heat fluxes are found in each region. For example, the values of sensible and latent heat flux along the line shown in Figures 5f and 5g may be representative of values taken along an aircraft flight path. These figures show that variations of a factor of 2 are common, even though they tend to average out over 20–30 km. *Lyons et al.* [2001] showed that you need to average the fluxes over at least 8 km to get a representative flux and this variability is a function of the underlying vegetation. For one 20-km-long aircraft flight leg over native vegetation at 1068 LT on 29 September 1992, latent heat fluxes averaged 134 W m^{-2}, while values of 281 W m^{-2} were found on another leg at 1010 LT on 5 October 1993 (note that the two measurements were taken in different years). These results demonstrate that the aircraft measurements can be highly variable even over the same time of year. Likewise, aircraft measurements between 1200 and 1300 LT show low and high values of sensible heat flux ranging from 96 to 205 W m^{-2} and from 144 to 292 W m^{-2} over agricultural and native vegetation regions, respectively, and values of latent heat flux ranging from 142 to 352 W m^{-2} and from 88 to 266 W m^{-2} over agricultural and native vegetation regions, respectively. Clearly, there is high variability in both the satellite and aircraft measurements, which may depend upon the exact flight path. The aircraft measurements are direct measurements of the fluxes via eddy correlation but are only representative of the flight path, i.e., [*Lyons et al.*, 2001], whereas satellite-derived measurements depend on the model used for inversion and have a coarser spatial resolution.

[58] Figure 11 also shows the diurnal variation of net available energy (sensible + latent) for native vegetation and agriculture regions. Note that the net available energy is nearly identical over both areas, except during the 1300–1400 LT period. While the reason for this is unknown, presence of upper layer cirrus cloudiness could have produced such an effect. Since the net available energy over both the areas is similar, the energy partitioning appears to be controlled by differences in vegetation type and soil moisture.

[59] By the summer month of December, due to an increase in incoming net radiation, there is an increase in the values of surface energy flux components over both agricultural and native vegetation areas. Due to lower albedo values, incoming net radiation is higher over the native vegetation. Also, there are significant changes in the way in which energy is partitioned in these areas. In the agricultural areas, lower surface moisture availability in combination with the absence of transpiring vegetation results in a higher portion of the incoming energy being used for warming the surface. However, the native vegetation area presents the reverse situation where higher soil moisture availability and presence of transpiring vegetation results in use of higher amount of net incoming energy for evaporating water. Thus in December, the surface temperatures and sensible heat fluxes are significantly higher for agricultural areas (318 K, 294 W m^{-2}, respectively) compared to native vegetation areas (312 K, 262 W m^{-2}, respectively). Note that this is a reversal of the situation found during the winter months. There is considerable difference in latent heat flux (84 W m^{-2}) between the areas, with higher latent heat fluxes over native vegetation areas. No comparisons with *Lyons et al.* [1993, 1996] and no aircraft data are available for this season.

[60] Differences in surface energy fluxes over agricultural and native vegetation are likely to be responsible for some of the observed differences in cloud formation over these areas, especially during the summer months. For the month of December, when the surface energy fluxes are significantly different between agricultural and native vegetation regions, the average cumulus cloud cover is higher over native vegetation (6.5%) compared to agricultural areas (3.8%). Note that for several days during the summer months, cumulus clouds are observed to form almost entirely over native vegetation areas and almost not at all over agricultural areas, an extreme case of which is shown in Figure 6d. On this day cumulus clouds form over the native vegetation, and the western boundary of the cumulus cloud field coincides very well with the native vegetation-agricultural boundary.

[61] In August the cumulus cloud cover (5.5%) is higher over agricultural areas compared to native vegetation (4.2%). This could be due to cloudiness from frequent frontal intrusions into the agricultural areas, which do not always extend into the native vegetation areas. There are some observed cases during the winter months in which clouds form preferentially over the agricultural areas and almost not at all over native vegetation areas. An example of this is shown in Figure 6b. However, reasons for this occasional preferential cloud formation over agricultural areas are not apparent at this point. This might be due to anomalous soil moisture patterns over the agricultural areas.

[62] To better understand the nature of regional climate change associated with clearing of native vegetation in the southwest Australian region, the surface energy budget for differing land use areas needs to be monitored over multiple seasons. Also, numerical modeling experiments involving land use change experiments could provide further insight into regional climate change in this region.

5. Conclusion

[63] This study has focused on the seasonal variations in land surface properties, cumulus cloudiness at hourly intervals from 0800 to 1500 LT, and cumulus cloud properties over Southwest Australia. Large homogeneous tracts of differing vegetation types are juxtaposed here, and the

boundary separating these two regions is sharp, with no significant topographical variations. This provides the opportunity to examine the effect of land use change upon climatological variables independent of other influences.

[64] Seasonal changes in land surface temperatures, albedos, and NDVI values over areas of agriculture and native vegetation are not similar. Available soil moisture fraction and surface energy fluxes show seasonal patterns, as do the maps of cumulus cloud occurrence. Values of NDVI, available soil moisture fraction, latent heat fluxes, and cumulus cloud frequencies are larger over native vegetation areas during the summer months, whereas values of albedo, land surface temperatures, and sensible heat fluxes are lower. Toward the end of the winter season, during the months of August and September the reverse is true. For example, ASTER results near the fence in September show that available fractional soil moisture average values are about 0.5 over agriculture areas compared to about 0.4 over native vegetation areas. However, in December native vegetation areas have fractional moisture availability values of about 0.12 compared to values of about 0.08 in the agricultural areas. Similarly, latent heat flux values are about 253 W m^{-2} over agricultural areas in September, compared with average values of 232 W m^{-2} for native vegetation areas. By December the agricultural areas have lower averages of latent heat fluxes of 142 W m^{-2}, whereas native vegetation areas average around 227 W m^{-2}. In contrast, sensible heat fluxes increase from 129 to 294 W m^{-2} over agricultural areas and from 137 to 262 W m^{-2} over native vegetation areas from September to December.

[65] Hourly maps of cumulus cloud frequency for August show that cumulus clouds have higher frequencies of occurrence over agricultural areas particularly between 0800 and 0900 LT and then again from 1300 to 1500 LT. Between 1000 and 1200 LT cumulus clouds do not show any preferential higher frequency of occurrence over either vegetation types in this month. The hourly maps of monthly cumulus cloudiness in November and December show higher cumulus frequency of occurrence over agricultural areas from 0800 to 1500 LT very close to the vermin fence, and over native vegetation from 1200 to 1500 LT. This pattern is distinctly visible for the months of December and January, but it is less noticeable for November.

[66] Cumulus cloud and optical and microphysical properties show similar seasonal changes. Cumulus clouds tend to be optically thicker over agricultural areas during September (agricultural season), but from October to December (summer months) the cloud optical thicknesses tend to be higher over regions of native vegetation. Cloud LWP also tends to be larger in August and September over agricultural areas, but from October to December LWP tends to be larger over native vegetation areas.

[67] During August cumulus clouds are spatially more extensive and occur with higher frequency over agricultural areas. During the dry season summer months of November through January, cumulus clouds have higher frequency of occurrence over native vegetation. Available soil moisture fraction and latent heat fluxes are also higher over native vegetation during the dry season months.

[68] **Acknowledgments.** This research was conducted under the EOS Advanced Spaceborne Thermal Emission and Reflection Radiometer (ASTER), NASA grant NAS5-31718, and the EOS Cloud and Earth's Radiant Energy Budget Scanner (CERES), and NASA contract NAS1-98131. We thank Toby Carlson for the SVAT model and Todd Berendes for the ASTER and MODIS calibration program and the IVICS codes.

References

Avissar, R., and Y. Liu, A three-dimensional numerical study of shallow convective clouds and precipitation induced by land-surface forcings, *J. Geophys. Res.*, *101*, 7499–7518, 1996.

Avissar, R., and T. Schmidt, An evaluation of scale at which ground-surface heat flux patchiness affects the convective boundary layer using large-eddy simulations, *J. Atmos. Sci.*, *55*, 2666–2689, 1998.

Berendes, T. A., R. M. Welch, U. S. Nair, and D. A. Berendes, Interactive visualizer and image classifier for satellites, *EOS Trans. AGU*, *82*(20), Spring Meet. Suppl., Abstract U21A-16, 2001.

Chou, J., R. C. Weger, J. M. Ligtenberg, P. Breeden, K.-S. Kuo, and R. M. Welch, Segmentation of polar scenes using multispectral texture measures and morphological filtering, *Int. J. Remote Sens.*, *15*, 1019–1036, 1994.

Cutrim, E. D., W. Martin, and R. Rabin, Enhancement of cumulus clouds over deforested lands in Amazonia, *Bull. Am. Meteorol. Soc.*, *76*, 1801–1805, 1995.

Gillies, R. R., and T. N. Carlson, Thermal remote sensing of surface soil water content with partial vegetation cover for incorporation into climate models, *J. Appl. Meteorol.*, *34*, 745–756, 1995.

Gillies, R. R., T. N. Carlson, J. Cui, W. P. Kustas, and K. S. Humes, A verification of the "triangle" method for obtaining surface soil water content and energy fluxes from remote measurements of the Normalized Difference Vegetation Index (NDVI) and surface radiant temperature, *Int. J. Remote Sens.*, *18*, 3145–3166, 1997.

Han, Q., Global survey of effective particle size in liquid water cloud by satellite observations, Ph.D. dissertation, 205 pp., Columbia Univ., New York, 1992.

Han, Q., W. B. Rossow, and A. A. Lacis, Near-global survey of effective droplet radii in liquid water clouds using ISCCP data, *J. Clim.*, *7*, 465–497, 1994.

Han, Q., W. Rossow, R. Welch, A. White, and J. Chou, Validation of satellite retrievals of cloud microphysics and liquid water path using observations from FIRE, *J. Atmos. Sci.*, *52*, 4183–4195, 1995.

Huang, X., T. J. Lyons, and R. C. G. Smith, Meteorological impact of replacing native perennial vegetation with annual agricultural species, *Hydrol. Processes*, *9*, 645–654, 1995.

Kuo, K.-S., R. M. Welch, and R. C. Weger, The three-dimensional structure of cumulus clouds over the ocean, 1, Structural analysis, *J. Geophys. Res.*, *98*, 20,685–20,711, 1993.

Levine, M. D., and S. I. Shaheen, A modular computer vision system for picture segmentation and interpretation, in *IEEE Transactions on Pattern Analysis and Machine Intelligence*, *PAMI-3*, 540–556, 1978.

Lynn, B. H., W.-K. Tao, and P. J. Wetzel, A study of landscape-generated deep moist convection, *Mon. Weather Rev.*, *126*, 928–942, 1998.

Lyons, T. J., Clouds prefer native vegetation, *Meteorol. Atmos. Phys.*, *80*, 131–140, 2002.

Lyons, T. J., P. Schwerdtfeger, J. M. Hacker, I. J. Foster, R. C. G. Smith, and H. Xinmei, Land-atmosphere interaction in a semiarid region: The bunny fence experiment, *Bull. Am. Meteorol. Soc.*, *74*, 1327–1334, 1993.

Lyons, T. J., R. C. G. Smith, and H. Xinmei, The impact of clearing for agriculture on the surface energy budget, *Int. J. Clim.*, *16*, 551–558, 1996.

Lyons, T. J., L. Fuqin, J. M. Hacker, W.-L. Cheng, and H. Xinmei, Regional turbulent statistics over contrasting natural surfaces, *Meteorol. Atmos. Phys.*, *78*, 183–194, 2001.

Meher-Homji, V. M., Probable impact of deforestation on hydrological processes, *Clim. Change*, *19*, 163–173, 1991.

Nair, U. S., J. A. Rushing, R. Ramachandran, K. S. Kuo, R. M. Welch, and S. J. Graves, Detection of cumulus cloud fields in satellite imagery, in *Earth Observing Systems IV*, vol. 3750, *Proceedings of SPIE*, edited by W. L. Barnes, pp. 345–355, 1999.

Pielke, R. A., Sr., Influence of the spatial distribution of vegetation and soils on the prediction of cumulus convective rainfall, *Rev. Geophy.*, *39*, 151–177, 2001.

Rabin, R. M., The surface energy budget of a summer convective period, M.S. thesis, McGill Univ., Montreal, Canada, 125 pp., 1977.

Rabin, R. M., and D. W. Martin, Satellite observations of shallow cumulus coverage over the central United States: An exploration of landuse impact on cloud cover, *J. Geophys. Res.*, *101*, 7149–7155, 1996.

Rabin, R. M., S. Stadler, P. J. Wetzel, D. J. Stensrud, and M. Gregory, Observed effect of landscape variability on convective clouds, *Bull. Am. Meteorol. Soc.*, *71*, 272–280, 1990.

Segal, M., R. Avissar, M. C. McCumber, and R. A. Pielke, Evaluation of vegetation effects on the generation and modification of mesoscale circulations, *J. Atmos. Sci.*, *45*, 2268–2292, 1988.

Segal, M., R. W. Arrit, C. Clark, R. Rabin, and J. Brown, Scaling evaluation of the effect of surface characteristics on potential for deep convection over uniform terrain, *Mon. Weather Rev.*, *123*, 383–400, 1995.

Su, W., J. Mao, J. Fei, and Q. Yu, Outgoing longwave radiation and cloud radiative forcing of the Tibetan Plateau, *J. Geophys. Res.*, *105*, 14,863–14,872, 2000.

Sud, Y. C., W. C. Chao, and G. K. Walker, Dependence of rainfall on vegetation: Theoretical considerations, simulation experiments, observations, and inferences from simulated atmospheric soundings, *J. Arid Environ.*, *25*, 5–18, 1993.

Twomey, S., M. Piepgrass, and T. L. Wolfe, An assessment of the impact of pollution on global cloud albedo, *Tellus, Ser. B*, *36*, 356–366, 1984.

Van de Hulst, H. C., *Multiple Light Scattering, Tables, Formulas, and Applications*, vols. 1 and 2, 739 pp., Academic, San Diego, Calif., 1980.

Weaver, C. P., and R. Avissar, Atmospheric disturbances caused by human modification of landscape, *Bull. Am. Meteorol. Soc.*, *82*, 269–282, 2001.

Zhong, S., and J. C. Doran, An evaluation of the importance of surface flux variability on GCM-scale boundary-layer characteristics using realistic meteorological and surface forcing, *J. Clim.*, *11*, 2774–2788, 1998.

Q. Han, U. S. Nair, D. K. Ray, R. M. Welch, and J. Zeng, Department of Atmospheric Sciences, University of Alabama in Huntsville, 320 Sparkman Drive, Huntsville, AL 35805, USA. (ray@nsstc.uah.edu)

T. Kikuchi, Department of Information Science, Kochi University, Kochi City, Japan.

T. J. Lyons, School of Environmental Science, Murdoch University, Murdoch, WA 6150, Australia.

W. Su, Center for Atmospheric Sciences, Hampton University, Hampton, VA 23681-2199, USA.